AIAA Aviation Forum and ASCEND co-located Conference Proceedings
29 July - 2 August 2024, Las Vegas, Nevada
AIAA AVIATION FORUM AND ASCEND 2024
10.2514/6.2024-3954

High-Order Upwind Multi-Layer Compact Scheme (MLC) with Shock-Fitting Method for Two-Dimensional Supersonic Flows

Yung-Tien Lin* and Xiaolin Zhong.†
University of California, Los Angeles, California, 90095

This paper implements the high-order multi-layer compact (MLC) scheme developed by Bai and Zhong (JCP, 2019) on two-dimensional supersonic flow and proposes a physically consistent shock-fitting method for MLC. MLC introduces the spatial derivatives as the method's new degrees of freedom and computes the time change of the derivatives based on the auxiliary equations. In Bai and Zhong's work, MLC can achieve seventh-order spatial accuracy globally with closed boundaries for linear advection problems, and the stability of the methods was investigated. In addition to the previous works, this paper implemented the MLC on non-Cartesian grids and incorporated it with arbitrary Lagrangian-Eulerian formulation for mesh movement. Also, the shock-fitting method is introduced to preserve the high-order spatial accuracy results in MLC by removing the discontinuous solutions across the shock wave. However, the state derivatives behind the shock wave require additional boundary conditions for the shock-fitting method. This study proposes a physically consistent boundary condition for these derivative layers by utilizing the time derivative of C^+ characteristics in the Rankine-Hugoniot conditions. The grid convergence rate studies on one-dimensional shock-density wave and two-dimensional vorticity-entropy shock interaction problems with this proposed approach are presented. The seventh-order MLC with the proposed boundary condition can achieve eighth-order spatial accuracy in the smooth region of the one-dimensional shock-density wave interaction problem and seventh-order accuracy for the two-dimensional shock interaction problem. In contrast, the conventional upwind finite difference method is around sixth-order accurate with a seventh-order interior scheme. The difference in spatial accuracy between the two methods results in a 1.32 times speedup for MLC in the global region and a 3.34 times speedup in the smooth region for the one-dimensional problem. This study aims to provide a framework for MLC simulating the two-dimensional supersonic flow over a blunt object. The ultimate application of this method is Direct Numerical Simulation (DNS) of supersonic boundary layer transition flow.

I. Nomenclature

a, b, c	=	MLC coefficients
$\vec{a}_G$	=	grid normal vector
b_G	=	grid normal velocity
e	=	total energy per unit mass
g	=	determinant of the coordinate transformation Jacobian
h	=	grid size
l, m	=	spatial wave number for the perturbed states
p	=	static pressure
t	=	time
r	=	order of spatial accuracy
u, U	=	state value
u, v, w	=	flow velocity in x, y, and z directions respectively
x, y, z	=	Cartesian coordinate in the physical domain
α	=	upwind parameter

*Ph.D. Student, Mechanical and Aerospace Engineering, yungtlin@g.ucla.edu, AIAA Student Member.
†Professor, Mechanical and Aerospace Engineering, xiaolin@seas.ucla.edu, AIAA Associate Fellow.

γ	=	ratio of ideal gas specific heat
ρ	=	density
δ	=	magnitude of density wave
ϵ	=	WENO local smoothness indicator
λ^+	=	state eigenvalue associated with C^+
ξ, η, ζ	=	Cartesian coordinate in the computational domain
θ	=	transform domain rotating angle
$\mathbf{A}$, $\mathbf{B}$	=	flux Jacobians for E and F respectively
$C^{\pm}$	=	characteristics propagated toward/away shockfront
E, F, G	=	fluxes in x, y, and z directions respectively
$\vec{F}$	=	flux vector
I^+	=	state eigenvector associated with C^+
M	=	Mach number
N	=	mesh number
Pr	=	Prandtl number
R	=	the radius of curvature at the parabola center
T	=	simulation time
U	=	flow states
Ω	=	computational domain

Superscripts and Subscripts

$p', u', v', \ldots$	=	perturbed states
A_v, A_e	=	perturbation amplitude for vorticity and entropy modes
$C^1, C^2, \ldots, C^\infty$	=	function smoothness
E', F', G'	=	fluxes in computational domain
$L^1, L^2, \ldots, L^\infty$	=	Lebesgue spaces
$\overline{p}, \overline{u}, \overline{v}, \ldots$	=	averaged states
x_G	=	shock location
x_w, y_w	=	parabolic wall location
u_1, u_2	=	upstream and downstream states
u_i, u_j	=	numerical solution indices
u_t	=	temporal differentiation
D_x, D_y	=	domain length in x and y direction
u_x, u_y, u_z	=	spatial differentiation with respect to x, y, and z
u_ξ, u_η, u_ζ	=	spatial differentiation with respect to ξ, η, and ζ
U_s	=	states right behind the shock
U_0	=	states right in front of the shock
U_∞	=	freestream states
Ω_1	=	the smooth region in one-dimensional shock-density wave interaction problem

II. Introduction

High-order numerical methods are computationally more efficient in smooth problems than low-order methods by using fewer grid points or degrees of freedom (DoF) to achieve the same order of accuracy [1]. Most of the high-order methods are based on polynomial approximation or use multiple basis functions to achieve the desired spatial accuracy. However, one of the most undesirable properties in high-order methods is numerical stability. For instance, in the conventional finite difference method, high-order schemes are obtained by using a wider stencil in simulations. The broad coverage of numerical stencils causes the simulation to be unstable and leads to diverged solutions. This stability issue becomes even worse when applied to flows involved with shocks or strong turbulence. To address this issue, researchers have come up with different approaches to achieve high-order simulation results for fluid mechanics problems.

In the hypersonic directed numerical simulation (DNS) community, several high-order schemes have been deployed, such as central-upwind finite difference [2, 3], the upwind finite difference with pseudo-spectral method [4], kinetic energy consistent (KEC) flux [5], and weighted essentially non-oscillatory (WENO) methods [6, 7]. Even though some of the above methods use seventh or even ninth-order interior schemes, the actual simulation results converge around fifth to sixth-order globally. One of the reasons is the stability requirement for the boundary closure schemes. For instance, a seventh-order upwind finite difference method requires a fifth-order boundary scheme near boundaries to remain stable but results in sixth-order accuracy globally [2].

In the recent works of Bai and Zhong [8–10], they proposed a method named the multi-layer compact (MLC) scheme. This method is based on the upwind central finite difference [2] and adds state derivatives as new degrees of freedom to the scheme. By utilizing both the value and derivatives layer, the resulting MLC stencil during the computation is narrower than the conventional finite difference method. The eigenvalue stability analysis shows that seventh-order MLC can be incorporated with sixth-order boundary schemes. This implies MLC has the potential to converge with seventh-order accuracy globally.

For this study, MLC will be applied to linear advection, Euler equations, and Navier-Stokes equations. In addition, for two-dimensional flow, a modified MLC named directional MLC (DMLC) [10] will be tested for linear advection. To suppress the Gibbs phenomenon around the shock, a shock-fitting method [2] is also applied to MLC. The testing results of this study show the capability of MLC on both one-dimensional and two-dimensional supersonic flow with a shock wave involved.

III. High-Order Upwind Multi-Layer Compact (MLC) Schemes

For three-dimensional fluid mechanics problems, the governing equation can be expressed in the following nonlinear advection form:

$$\frac{\partial U}{\partial t} + \frac{\partial E}{\partial x} + \frac{\partial F}{\partial y} + \frac{\partial G}{\partial z} = 0 \tag{1}$$

For Euler equations, the states and fluxes are:

$$U = \begin{bmatrix} \rho \\ \rho u \\ \rho v \\ \rho w \\ \rho e \end{bmatrix}, \qquad E = \begin{bmatrix} \rho u \\ \rho u^2 + p \\ \rho uv \\ \rho uw \\ (\rho e + p)u \end{bmatrix}, \qquad F = \begin{bmatrix} \rho v \\ \rho uv \\ \rho v^2 + p \\ \rho uw \\ (\rho e + p)v \end{bmatrix}, \qquad G = \begin{bmatrix} \rho w \\ \rho uw \\ \rho vw \\ \rho w^2 + p \\ (\rho e + p)w \end{bmatrix} \tag{2}$$

and for the Navier-Stokes equations, one can obtain the expression by introducing the viscous and thermal conduction terms into the above formulation.

In the following sections, the multi-layer compact (MLC) scheme will be based on the above equation to derive the auxiliary equations for the derivatives layer in one-dimensional and two-dimensional problems.

A. One Dimensional Formulation

The fundamental idea of the MLC is to add additional degrees of freedom for each grid point. Spatial derivatives of the flow states are selected as extra simulated variables since they have a direct relation with flux derivatives. To obtain the auxiliary equations for the newly introduced variables, one can utilize spatial differentiation of the original governing equation. For example, in one dimensional MLC problem, Eq. (1) becomes:

$$\frac{\partial}{\partial t}\begin{bmatrix} U \\ U_x \end{bmatrix} + \frac{\partial}{\partial x}\begin{bmatrix} E \\ E_x \end{bmatrix} = 0 \tag{3}$$

The flux derivative with respect to x, $\partial E/\partial x = E_x$, has a direct relation with U_x by using the flux Jacobian, i.e., $E_x = \mathbf{A}U_x$. Hence the only remaining unknown in Eq. (3) is the flux's second derivative, E_{xx}. In MLC, the second derivative of a numerical state u can be approximated by using neighboring values of u and u_x:

$$(u_{xx})_i = \frac{1}{h^2}\sum_{l=-L_1}^{L_2} a_l u_{i+l} + \frac{1}{h}\sum_{m=-M_1}^{M_2} b_m (u_x)_{i+m} + O(h^r) \tag{4}$$

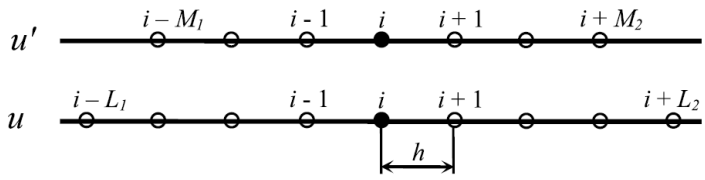

Fig. 1 Schematic of $L_1 - L_2 - M_1 - M_2$ scheme for MLC second-derivative approximation.

The above MLC coefficients, a and b, can be derived from the Taylor series with a uniform grid size, h. Fig. 1 shows the schematic of the stencil used in the above equation with $L_1 - L_2 - M_1 - M_2$. For instance, the seventh-order MLC coefficients with the upwind parameter, α, to stabilize the numerical scheme for hyperbolic equations:

$$\begin{aligned} a_{\pm 2} &= \frac{7}{85} \mp \frac{25}{3456}\alpha, & a_{\pm 1} &= \frac{64}{27} \mp \frac{5}{108}\alpha, & a_0 &= -5 \\ b_{\pm 2} &= \mp\frac{1}{36} + \frac{1}{576}\alpha, & b_{\pm 1} &= \mp\frac{8}{9} + \frac{1}{36}\alpha, & b_0 &= \frac{1}{16}\alpha \end{aligned} \tag{5}$$

For the actual value of the third and fifth-order MLC coefficients, Bai and Zhong's study [8] provides a more detailed derivation process and the definition of the upwind parameter. In this study, the upwind parameters for different orders of accuracy are given in Table 1 which are the same values provided in Bai and Zhong's stability study. With the above formulations, the flux's second derivative, E_{xx}, in Eq. (3) can be approximated by the MLC scheme by evaluating from E and E_x. Then the equation can be applied with a time integration method to simulate the one-dimensional problem.

Table 1 MLC spatial accuracy and corresponding upwind parameter.

MLC Scheme	Order of Accuracy, r	Upwind Parameter, α
1-1-1-1	3	1.5
2-2-1-1	5	-1
2-2-2-2	7	12

B. Two Dimensional Formulation

For two dimensional MLC problem, Eq. (1) becomes:

$$\frac{\partial}{\partial t}\begin{bmatrix} U \\ U_x \\ U_y \end{bmatrix} + \frac{\partial}{\partial x}\begin{bmatrix} E \\ E_x \\ E_y \end{bmatrix} + \frac{\partial}{\partial y}\begin{bmatrix} F \\ F_x \\ F_y \end{bmatrix} = 0 \tag{6}$$

Similar to the one-dimensional problem, the first derivatives of fluxes are derived from flux Jacobians and the second derivatives, E_{xx} and F_{yy}, can be approximated by Eq. (4). So the remaining unknowns in the two-dimensional equation are second-order mixed derivative terms, E_{xy} and F_{xy}. The mixed derivative, u_{xy}, can be approximated by using u, u_x and u_y:

$$\begin{aligned} (u_{xy})_{ij} = &\frac{1}{h^2}\sum_{l_y=L_1}^{L_2}\sum_{l_x=L_1}^{L_2} a_{l_x,l_y} u_{i+l_x,j+l_y} \\ &+ \frac{1}{h}\sum_{m_y=M_1}^{M_2}\sum_{m_x=M_1}^{M_2}\left[b_{m_x,m_y}(u_x)_{i+m_x,j+m_y} + c_{m_x,m_y}(u_y)_{i+m_x,j+m_y}\right] + O(h^r) \end{aligned} \tag{7}$$

Noting that most of the coefficients inside the stencil remain zero; only a few of the points have non-zero values. This is due to the two-dimensional stencil involving too many points than the required number to achieve targeting accuracy. The point selection process is based on using as few points as possible to reduce the computational cost and suppress round-off error accumulation. For simplicity, the detailed point selection process and actual coefficient values are left in Bai and Zhong's study [8].

C. Directional Multi-Layer Compact (DMLC) Scheme

However, the above mixed derivative approximation will have weak numerical instabilities for a small range of wavenumbers [9]. To address this issue, Bai and Zhong proposed another approach [10] to solve the mixed derivative instability in multi-dimensional MLC. This approach is called the directional multi-layer compact (DMLC) scheme which introduces cross derivatives as new unknowns. For instance, Eq. (6) in DMLC becomes:

$$\frac{\partial}{\partial t}\begin{bmatrix} U \\ U_x \\ U_y \\ U_{xy} \end{bmatrix} + \frac{\partial}{\partial x}\begin{bmatrix} E \\ E_x \\ E_y \\ E_{xy} \end{bmatrix} + \frac{\partial}{\partial y}\begin{bmatrix} F \\ F_x \\ F_y \\ F_{xy} \end{bmatrix} = 0 \tag{8}$$

With the introduction of U_{xy} to the system, one can use the flux Jacobian and the chain rule to obtain E_{xy} and F_{xy}, e.g., $E_{xy} = \mathbf{A}_y U_x + \mathbf{A} U_{xy}$. Hence, the remaining unknowns in the system are the third-order derivative E_{xxy} and F_{xyy}. However, these terms can be solved by using the one-dimensional MLC approximation. For instance, E_{xxy} is approximated by E_y and E_{xy} in x direction and, similarly, F_{xyy} is approximated by F_x and F_{xy} in y direction. So the above process avoids DMLC using the unstable cross-derivative approximation and yields more stable results. In the numerical results section, both MLC and DMLC will be discussed and compared for two-dimensional problems.

IV. Shock-Fitting Method

A. Moving Mesh Treatment

The shock-fitting method implemented in this study is based on Zhong's work [2]. In this approach, shockfront is treated as a fixed boundary in the computational domain and grid points are moving in the physical domain. Therefore, Eq. (1) needs to be revised to incorporate the moving mesh. One of the approaches is to apply the arbitrary Lagrangian-Eulerian method to the governing equation and have:

$$\frac{\partial g U}{\partial t} + \frac{\partial E'}{\partial \xi} + \frac{\partial F'}{\partial \eta} + \frac{\partial G'}{\partial \zeta} = 0 \tag{9}$$

where

$$\begin{bmatrix} E' \\ F' \\ G' \end{bmatrix} = g\begin{bmatrix} \xi_x & \xi_y & \xi_z \\ \eta_x & \eta_y & \eta_z \\ \zeta_x & \zeta_y & \zeta_z \end{bmatrix}\begin{bmatrix} E \\ F \\ G \end{bmatrix} + g\begin{bmatrix} \xi_t \\ \eta_t \\ \zeta_t \end{bmatrix} U \tag{10}$$

The detailed derivation process in vector form can be checked by Persson et al [11]. The MLC form of the moving mesh treatment can be simply obtained by applying spatial derivative to the above equation. For two-dimensional MLC, U_ξ and U_η are used in derivative layers instead of using U_x and U_y. This is because using derivatives based on the physical domain will drop extra terms when deriving MLC equations in the computational domain due to the chain rule.

B. Shockfront Movement

With given free-stream conditions, the flow states right behind the shockfront can be computed through the Rankine–Hugoniot conditions:

$$\left(\vec{F}_s - \vec{F}_0\right) \cdot \vec{a}_G + (U_s - U_0)\, b_G = 0 \tag{11}$$

where $\vec{a}_G$ acts as the normal vector of the shockfront and b_G is a transformed shockfront normal velocity. If the shockfront is located at the top boundary on the computational domain, i.e. $\eta = 1$, then $\vec{a}_G$ and b_G are equal to:

$$\begin{aligned} \vec{a}_G &= (g\eta_x)_G \hat{x} + (g\eta_x)_G \hat{y} + (g\eta_x)_G \hat{z} \\ b_G &= g\eta_t \end{aligned} \tag{12}$$

Note that the time derivative of $\vec{a}_G$ can be considered as a function of b_G, since the location of shockfront is associated with the time integration of shock velocity.

However, there are several ways to evaluate the shockfront velocity. In Rawat and Zhong's study [12], three different shock velocity evaluation methods are discussed. Among the methods, the time derivative of the Rankine-Hugoniot conditions with C^+ characteristics has the best spatial accuracy when applied to the shock-fitting method with high-order finite difference methods. The method computes the shockfront velocity through time integration of shock acceleration and the acceleration is driven by Eq. (16).

The acceleration equation derivation starts with the time derivative of the Rankine-Hugoniot conditions:

$$\left(\frac{\partial \vec{F}_s}{\partial t} - \frac{\partial \vec{F}_0}{\partial t}\right) \cdot \vec{a}_G + \left(\vec{F}_s - \vec{F}_0\right) \cdot \frac{\partial \vec{a}_G}{\partial t} + \left(\frac{\partial U_s}{\partial t} - \frac{\partial U_0}{\partial t}\right) b_G + (U_s - U_0) \frac{\partial b_G}{\partial t} = 0 \tag{13}$$

Since the shockfront is defined at the top boundary of the computational domain, one only needs to consider the flux along the η direction, i.e., F'. The corresponding flux Jacobian for F':

$$\mathbf{B}' = \frac{\partial F'}{\partial U} \tag{14}$$

Substitute $\mathbf{B}'$ into Eq. (13):

$$\mathbf{B}'_s \frac{\partial U_s}{\partial t} - \mathbf{B}'_0 \frac{\partial U_0}{\partial t} + \left(\vec{F}_s - \vec{F}_0\right) \cdot \frac{\partial \vec{a}_G}{\partial t} + (U_s - U_0) \frac{\partial b_G}{\partial t} = 0 \tag{15}$$

Then compute the eigenvalue and eigenvector for the flux Jacobian right behind the shockfront, $\mathbf{B}'_s$. There exists an eigenvalue, λ_s^+, and an eigenvector, I_s^+, which is associated with the C^+ characteristic line that propagated toward the shockfront. Finally, inner product Eq. (15) with I_s^+ then obtain the shock acceleration equation:

$$\frac{\partial b_G}{\partial t} = \frac{-1}{[I_s^+ \cdot (U_s - U_0)]} \left[\lambda_s^+ I_s^+ \frac{\partial U_s}{\partial t} + I_s^+ (\vec{F}_s - \vec{F}_0) \cdot \frac{\partial \vec{a}_G}{\partial t} - (I_s^+ \mathbf{B}'_0) \frac{\partial U_0}{\partial t}\right] \tag{16}$$

With the acceleration of the shockfront, the shock velocity and location can be obtained through a time integration method.

C. MLC Adaptation

For the shock-fitting method on MLC, the flow states right behind the shock, U_s, are derived from Eq. (11) but the state derivatives remain undetermined. To ensure the MLC derivative layers' boundary condition is consistent with the above shock acceleration computation, this study adopts the same idea of using Rankine-Hugoniot conditions and flow characteristics. To simplify the deriving procedure, two-dimensional Euler equations are used and the shockfront tangential and normal directions are ξ and η respectively.

For the derivative layer tangential to the shockfront surface, $(U_\xi)_s$, the derivative can be directly derived from the spatial differentiation of Eq. (11), the Rankine–Hugoniot conditions:

$$\left(\vec{F}_s \cdot \vec{a}_G + U_s b_G\right)_\xi = \left(\vec{F}_0 \cdot \vec{a}_G - U_0 b_G\right)_\xi \tag{17}$$

This is due to the flow states behind the shock being derived from the upstream condition and shockfront geometry. Hence, the derivatives along the shockfront surface are independent of the downstream flow states.

For the derivative layers in the shockfront normal direction, $(U_\eta)_s$, the boundary condition deriving process starts from rearranging Eq. (15):

$$\frac{\partial U_s}{\partial t} = {\mathbf{B}'_s}^{-1} \left[\mathbf{B}'_0 \frac{\partial U_0}{\partial t} - \left(\vec{F}_s - \vec{F}_0\right) \cdot \frac{\partial \vec{a}_G}{\partial t} - (U_s - U_0) \frac{\partial b_G}{\partial t}\right] \tag{18}$$

Then the time derivative of the flow states is obtained and the spatial derivative of the flow state, $(U_\eta)_s$, can be acquired from the inverse of the Euler equations with flow Jacobians:

$$\frac{\partial U_s}{\partial \eta} = -{\mathbf{B}'_s}^{-1} \left(\frac{\partial U_s}{\partial t} + \mathbf{A}'_s \frac{\partial U_s}{\partial \xi}\right) \tag{19}$$

The physical meaning of the above process is utilizing the wave propagation direction in flow characteristics. In Eq. (16), the shock acceleration depends on the time derivatives associated with the C^+ characteristics line. This is due to C^+ being the only characteristic conveying information toward the shockfront. The rest of the characteristics, which originated from the shockfront, should depend on upstream states. Hence, Eq. (18) implicitly computes the rest of state derivatives with state derivatives associated with C^+ fixed. This new boundary condition at shockfront provides more accurate and numerically stable results than merely using interpolation. The results of this method are shown in the one-dimensional shock-density wave test. For the Navier-Stokes equations, Eq. (19) needs to be revised to incorporate the viscous effect into the state inversion process.

V. Numerical Results

In the following section, three advection problems will be discussed and tested by the conventional upwind finite difference (FD) method [2] and the upwind MLC [8] in the fifth and seventh-order formulation and applied with the shock-fitting method if possible. For one-dimensional problems, weighted essentially non-oscillatory (WENO) schemes are used for comparing with the fifth-order methods and represent results using the shock-capturing technique. The compared WENO methods are WENO5-JS [13], WENO5-M [14], and WENO5-Z [15]. The details of parameters used in WENO methods for the tests will be discussed in the one-dimensional linear advection problem. For the two-dimensional problem, DMLC will also be discussed. The time integration method for the three simulation cases is the standard fourth-order Runge-Kutta method. The time step is set to be sufficiently small to remove temporal errors and the corresponding Courant–Friedrichs–Lewy (CFL) number for the numerical tests ranges from 0.001 to 0.01. For Euler equations, the local Lax-Fridrich method [2] is used for flux splitting. In addition to the above grid convergence rate studies, a preliminary result of MLC with the 1-1-1-1 scheme for the two-dimensional supersonic flow over a cylinder is also presented. Even though MLC still requires further study on the viscous wall boundary conditions for the derivative layers, the result shows that the current implementation can converge to a proper solution which demonstrates the potential of the method on real applications.

A. One-Dimensional Linear Advection

The one-dimensional linear advection problem with periodic boundaries from Henrick et al [14] is given as follows:

$$\frac{\partial u}{\partial t} + \frac{\partial u}{\partial x} = 0 \quad \text{on } x \in [-1, 1], \quad t \in [0, 2] \tag{20}$$

and the initial condition:

$$u(x, t = 0) = sin\left(\pi x - \frac{sin(\pi x)}{\pi}\right) \tag{21}$$

The problem is designed to examine WENO methods when the first derivative vanishing points existed in the system. From Henrick et al [14] works, WENO5-JS has convergence issues near the vanishing point even though the solution is considered smooth. Hence, both WENO-M and WENO-Z are designed to address this issue and converge with optimal spatial accuracy. The parameter, ϵ, of WENO local smoothness indicator in WENO5-JS is set to 10^{-6} and for WENO5-M and WENO5-Z are 10^{-40}.

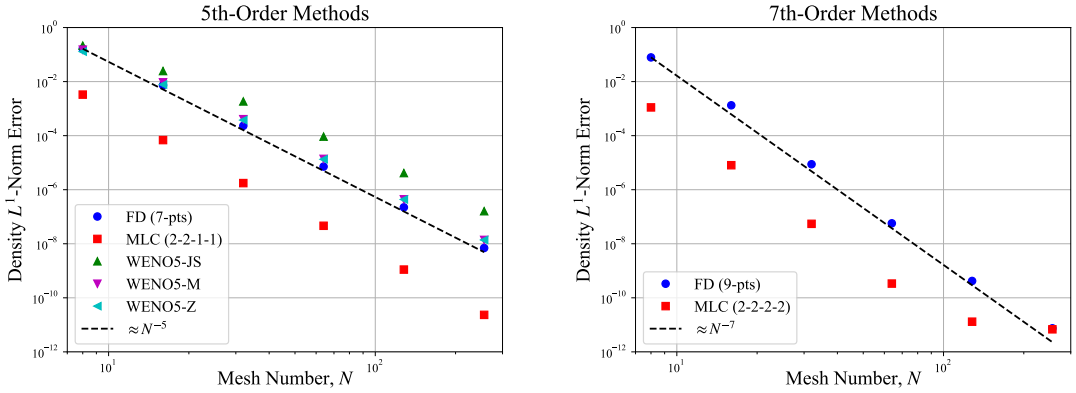

Fig. 2 One-dimensional linear advection: L^1-norm error versus mesh number N for fifth (left) and seventh-order (right) methods.

Fig. 2 shows the L^1-norm error convergence rate versus the mesh number, N, for fifth and seventh-order results. In fifth-order methods, WENO5-JS has the slowest convergence rate compared with the other four methods. This is due to the aforementioned convergence property in WENO5-JS. In contrast, WENO5-M and WENO-Z are able to converge in fifth-order accuracy which is the optimal convergence rate. One of the notable differences between these two methods is the computational cost. WENO-Z requires 30% less computing time than WENO-M [15]. This is due to WENO-Z using the absolute difference to re-evaluate smoothness indicators instead of remapping weights for each indicator. For the non-shock-capturing methods, the upwind finite difference method provides a steady fifth-order convergence rate and the error is slightly lower than the modified WENO methods for the same mesh number. For MLC, the method has the best overall spatial accuracy. One of the reasons is that MLC has two times of degrees of freedom than the other methods for the same grid points. However, even if the MLC result is shifted to match the degrees of freedom with other methods, the error of MLC is still lower than the others. The superior spatial accuracy in MLC also happened in seventh-order results. The one-dimensional linear advection problem shows the capability of the MLC with smooth solutions.

B. One-Dimensional Shock-Density Wave Interaction

The one-dimensional shock-density wave interaction presented in this study is based on Shu-Osher's problem [16] and revised by Suresh [17] for improving problem smoothness. The problem simulates a normal shock moving at Mach number, M, relative to the upstream and interacting with a density wave. The governing equations are the Euler equations:

$$\frac{\partial}{\partial t}\begin{bmatrix}\rho\\ \rho u\\ \rho e\end{bmatrix}+\frac{\partial}{\partial x}\begin{bmatrix}\rho u\\ \rho u^2+p\\ (\rho e+p)u\end{bmatrix}=0 \quad \text{on } x\in[-1,1], \quad t\in[0,0.36] \tag{22}$$

with the initial condition for downstream, $x \le x_G$:

$$\begin{aligned}\rho(x,t=0)&=\left[(\gamma+1)M^2\right]/\left[(\gamma-1)M^2+2\right]\\ u(x,t=0)&=\left[2\sqrt{\gamma}(M^2-1)\right]/\left[(\gamma+1)M\right]\\ p(x,t=0)&=1+\left[2\gamma(M^2-1)\right]/(\gamma+1)\end{aligned} \tag{23}$$

and for upstream, $x > x_G$:

$$\begin{aligned}\rho(x,t=0)&=1.0+\delta\cdot\sin^4(2.5\pi x)\\ u(x,t=0)&=0\\ p(x,t=0)&=1\end{aligned} \tag{24}$$

where $\gamma = 1.4$, $M = 3$, $\delta = 0.2$ and $x_G = -0.8$. The problem selected is due to fluxes relative to the shockfront being C^3 continuous when $t = 0$. This smoothness property provides a more gentle start for the density interaction process and yields a better convergence rate for high-order methods with the shock-fitting method.

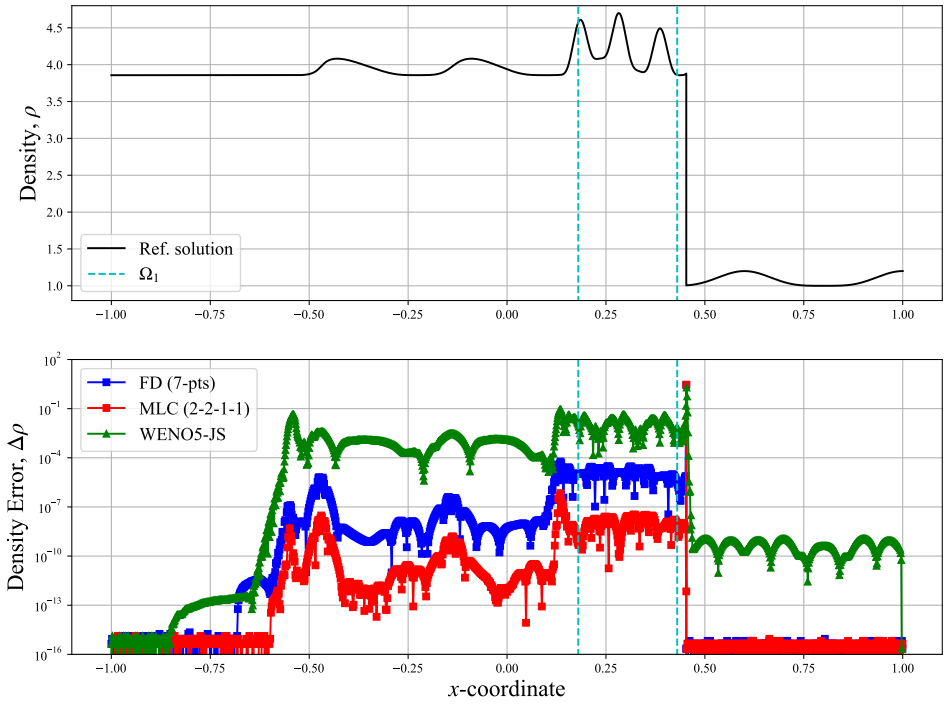

Fig. 3 One-dimensional shock-density wave interaction: density distribution at t = 0.36 (top) and the corresponding density error distribution for fifth-order methods.

Fig. 3 shows the simulation results of mesh number $N = 1,600$ for fifth-order FD, MLC, and WENO5-JS. The reference solution is from fifth-order FD with $N = 102,400$. From the density error distribution plot, a smooth region, Ω_1, is defined with $x \in [0.18, 0.43]$. This region will be used for error evaluation in the later part of this test. Also, the "global" error is defined by $x \in [-1, 0.43]$ to avoid errors near the shock.

Table 2 Global density L^1-norm error and convergence rate for fifth-order methods.

	FD (7-pts)		MLC (2-2-1-1)		WENO5-JS		WENO5-M		WENO5-Z	
N	L^1 error	r	L^1 error	r	L^1 error	r	L^1 error	r	L^1 error	r
50	$3.43 \cdot 10^{-2}$		$6.21 \cdot 10^{-3}$		$4.91 \cdot 10^{-2}$		$4.79 \cdot 10^{-2}$		$4.85 \cdot 10^{-2}$	
100	$1.24 \cdot 10^{-2}$	1.5	$4.65 \cdot 10^{-4}$	3.7	$2.48 \cdot 10^{-2}$	1.0	$2.88 \cdot 10^{-2}$	0.7	$2.82 \cdot 10^{-2}$	0.8
200	$1.86 \cdot 10^{-3}$	2.7	$1.00 \cdot 10^{-5}$	5.5	$1.02 \cdot 10^{-2}$	1.3	$1.25 \cdot 10^{-2}$	1.2	$1.14 \cdot 10^{-2}$	1.3
400	$8.58 \cdot 10^{-5}$	4.4	$2.23 \cdot 10^{-7}$	5.5	$4.13 \cdot 10^{-3}$	1.3	$5.24 \cdot 10^{-3}$	1.3	$4.31 \cdot 10^{-3}$	1.4
800	$3.04 \cdot 10^{-6}$	4.8	$5.79 \cdot 10^{-9}$	5.3	$1.58 \cdot 10^{-3}$	1.4	$2.06 \cdot 10^{-3}$	1.3	$1.63 \cdot 10^{-3}$	1.4
1600	$1.05 \cdot 10^{-7}$	4.9	$2.06 \cdot 10^{-10}$	4.8	$6.85 \cdot 10^{-4}$	1.2	$8.55 \cdot 10^{-4}$	1.3	$6.90 \cdot 10^{-4}$	1.2
3200	$3.78 \cdot 10^{-9}$	4.8	$1.01 \cdot 10^{-11}$	4.4	$3.13 \cdot 10^{-4}$	1.1	$3.66 \cdot 10^{-4}$	1.2	$3.19 \cdot 10^{-4}$	1.1

Table 3 Smooth region (Ω_1) density L^1-norm error in and convergence rate for fifth-order methods.

	FD (7-pts)		MLC (2-2-1-1)		WENO5-JS		WENO5-M		WENO5-Z	
N	L^1 error	r	L^1 error	r	L^1 error	r	L^1 error	r	L^1 error	r
50	$1.70 \cdot 10^{-1}$		$3.36 \cdot 10^{-2}$		$2.54 \cdot 10^{-1}$		$2.61 \cdot 10^{-1}$		$2.57 \cdot 10^{-1}$	
100	$5.50 \cdot 10^{-2}$	1.6	$2.30 \cdot 10^{-3}$	3.9	$2.04 \cdot 10^{-1}$	0.3	$2.03 \cdot 10^{-1}$	0.4	$2.03 \cdot 10^{-1}$	0.3
200	$8.84 \cdot 10^{-3}$	2.6	$4.55 \cdot 10^{-5}$	5.7	$9.06 \cdot 10^{-2}$	1.2	$1.14 \cdot 10^{-1}$	0.8	$1.08 \cdot 10^{-1}$	0.9
400	$3.82 \cdot 10^{-4}$	4.5	$7.80 \cdot 10^{-7}$	5.9	$3.29 \cdot 10^{-2}$	1.5	$4.56 \cdot 10^{-2}$	1.3	$3.89 \cdot 10^{-2}$	1.5
800	$1.29 \cdot 10^{-5}$	4.9	$1.26 \cdot 10^{-8}$	5.9	$1.02 \cdot 10^{-2}$	1.7	$1.72 \cdot 10^{-2}$	1.4	$1.19 \cdot 10^{-2}$	1.7
1600	$4.12 \cdot 10^{-7}$	5.0	$2.00 \cdot 10^{-10}$	6.0	$2.83 \cdot 10^{-3}$	1.9	$5.46 \cdot 10^{-3}$	1.7	$3.15 \cdot 10^{-3}$	1.9
3200	$1.30 \cdot 10^{-8}$	5.0	$3.04 \cdot 10^{-12}$	6.0	$8.18 \cdot 10^{-4}$	1.8	$1.57 \cdot 10^{-3}$	1.8	$8.96 \cdot 10^{-4}$	1.8

Table 2 shows the global density L^1-norm error for the fifth-order methods. For the shock-fitting methods, the upwind finite difference method converges around fifth-order and MLC can achieve a convergence rate with $r = 5.5$ in certain points. In contrast, the fifth-order shock-capturing schemes, without shock-fitting applied, are converged around first-order even for the two advanced WENO methods. Table 3 shows the error convergence rate of fifth-order methods in the smooth region, Ω_1. For the shock-fitting methods, the upwind finite difference method achieves fifth-order accuracy faster than the global error and MLC's convergence rate is capped at sixth-order. On the other hand, WENO methods' performance is improved but still below second-order.

Table 4 Global and the smooth region density L^1-norm error and convergence rate for seventh-order methods.

	Global				Smooth Region			
	FD (9-pts)		MLC (2-2-2-2)		FD (9-pts)		MLC (2-2-2-2)	
N	L^1 error	r	L^1 error	r	L^1 error	r	L^1 error	r
50	$4.45 \cdot 10^{-2}$		$8.50 \cdot 10^{-3}$		$2.47 \cdot 10^{-1}$		$4.62 \cdot 10^{-2}$	
100	$8.10 \cdot 10^{-3}$	2.5	$1.82 \cdot 10^{-4}$	5.5	$4.18 \cdot 10^{-2}$	2.6	$7.15 \cdot 10^{-4}$	6.0
200	$2.45 \cdot 10^{-4}$	5.1	$2.10 \cdot 10^{-6}$	6.4	$1.13 \cdot 10^{-3}$	5.2	$3.47 \cdot 10^{-6}$	7.7
400	$4.63 \cdot 10^{-6}$	5.7	$5.92 \cdot 10^{-8}$	5.1	$1.92 \cdot 10^{-5}$	5.9	$1.22 \cdot 10^{-8}$	8.2
800	$9.48 \cdot 10^{-8}$	5.6	$1.75 \cdot 10^{-9}$	5.1	$2.75 \cdot 10^{-7}$	6.1	$4.69 \cdot 10^{-11}$	8.0
1600	$2.80 \cdot 10^{-9}$	5.1	$9.31 \cdot 10^{-11}$	4.2	$3.77 \cdot 10^{-9}$	6.2	$1.82 \cdot 10^{-12}$	4.7
3200	$1.19 \cdot 10^{-10}$	4.6	$5.21 \cdot 10^{-12}$	4.2	$5.45 \cdot 10^{-11}$	6.1	$8.69 \cdot 10^{-13}$	1.1

For seventh-order methods, Table 4 shows the L^1-norm error in both global and smooth regions. Both the upwind finite difference method and MLC are below seventh-order accuracy in the global region. One of the possible reasons for the reduction in spatial accuracy is the upstream flux is C^3 continuous across the shock. The discontinuity in higher-order derivatives causes the high-order approximation to fail and leads to incorrect derivative estimation. The error due to the discontinuity can be observed in Fig. 3 at the interfaces of different system waves (x around -0.5 and 0.2). One way to reduce the discontinuity error is using C^∞ function in the upstream such as the bump function. Nevertheless, the spatial accuracy is recovered when the seventh-order methods in the smooth region, Ω_1. The upwind finite difference method is capped at sixth-order accuracy due to the usage of the fifth-order boundary closure scheme for stability. In contrast, MLC can even reach an eighth-order convergence rate with the proposed boundary condition and eventually reduce to first-order due to the emergence of truncation errors.

Regarding computational efficiency, Fig. 4 and Fig. 5 show the L^1-norm error in the global and smooth regions concerning the mesh number, degrees of freedom, and elapsed time. Either in the plots of degrees of freedom or elapsed time, MLC is the fastest method in converging errors. This implies MLC is the most memory and computing time-efficient method among the compared methods. In seventh-order methods, the upwind finite difference method requires 162.7 seconds to achieve an error of 10^{-10} in the global and smooth regions. On the other hand, MLC only took 122.4 and 48.7 seconds to reach the error for global and smooth regions respectively. In other words, MLC provides a 1.32 times speedup in the global region and 3.34 times speedup in the smooth region over the upwind finite difference

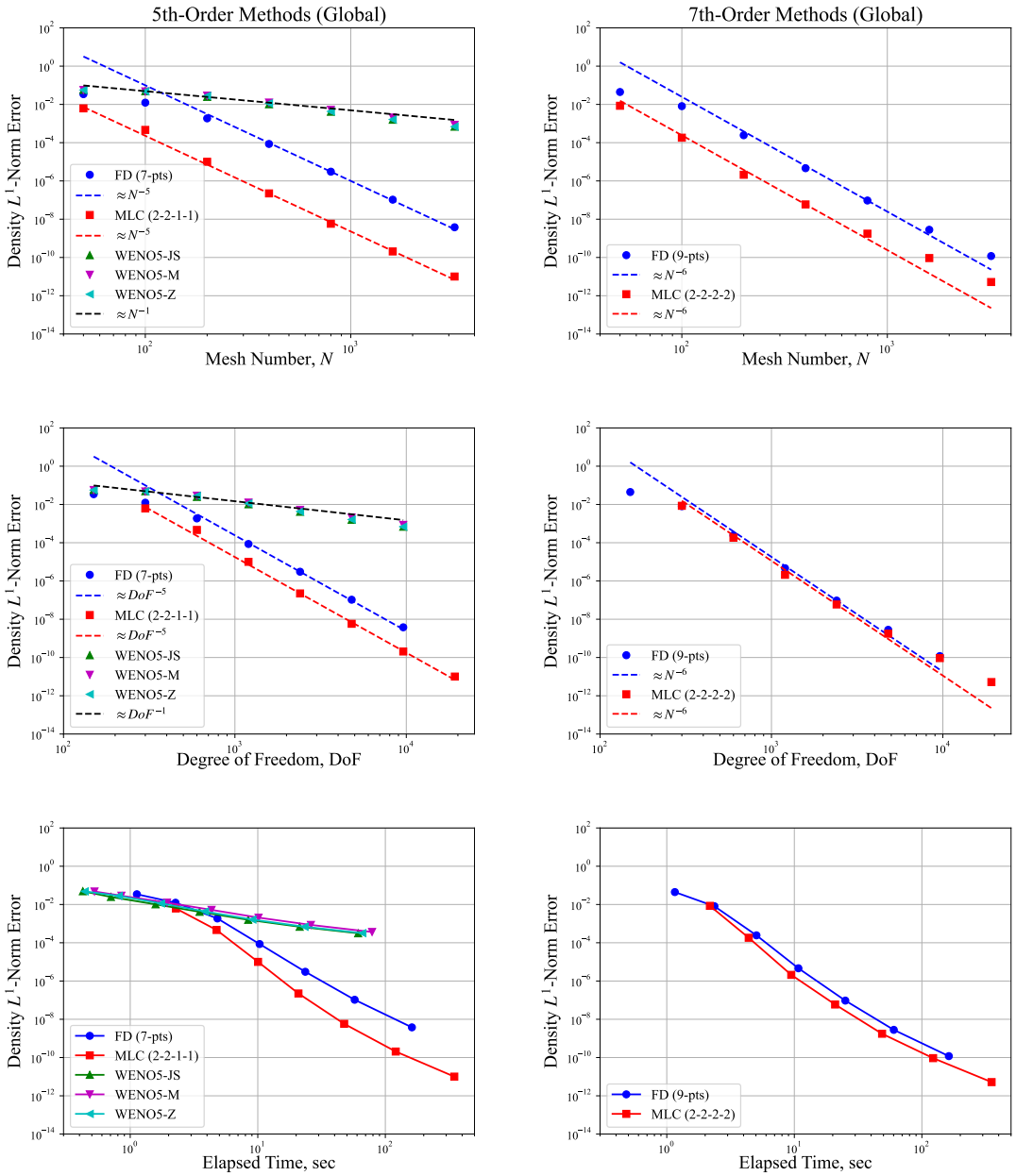

Fig. 4 One-dimensional shock-density wave interaction: global L^1-norm error versus mesh number N (top), degrees of freedom (middle), and computing elapsed time (bottom) for fifth (left) and seventh-order (right) methods.

for obtaining density L^1-norm error equal to 10^{-10}.

C. Two-dimensional Linear Advection with Moving Mesh

The two-dimensional linear advection with moving mesh problem aims to verify MLC and DMLC with a two-dimensional advection equation with moving mesh treatment. The problem is given as a rectangular computational domain with a tilt angle $\theta = 30°$ and the entire domain is moving uniformly in $\vec{v} = (-1, -1)$. The governing equation

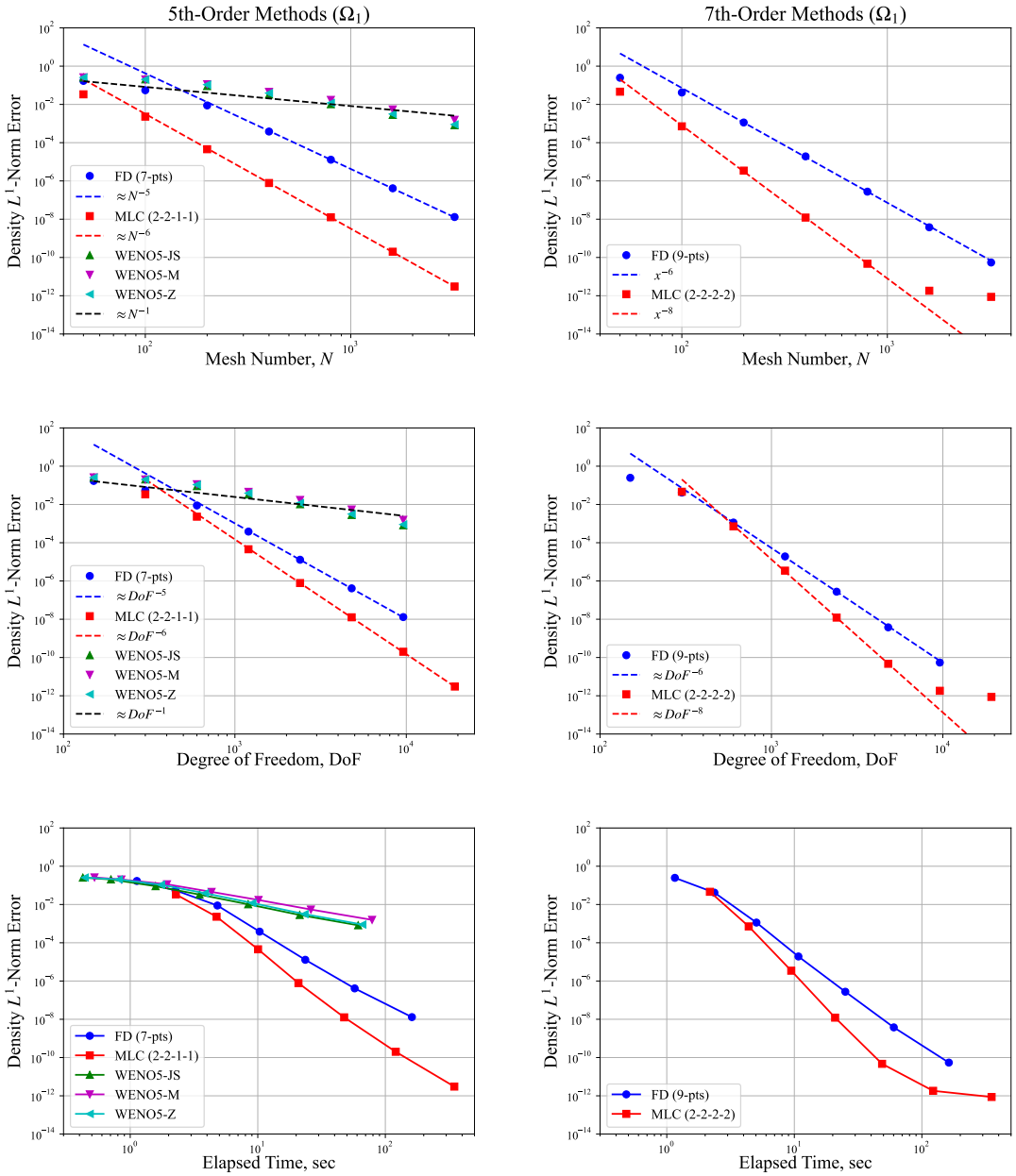

Fig. 5 One-dimensional shock-density wave interaction: L^1-norm error in the smooth region, Ω_1, versus mesh number N (top), degrees of freedom (middle), and computing elapsed time (bottom) for fifth (left) and seventh-order (right) methods.

for this problem can be derived from Eq. (9):

$$\frac{\partial gU}{\partial t} + \frac{\partial E'}{\partial \xi} + \frac{\partial F'}{\partial \eta} = 0 \quad \text{on } \xi, \eta \in [0,1], \quad t \in [0,1] \tag{25}$$

where the state and fluxes in the physical domain are $U = E = F = u$. For the initial condition:

$$u(x, y, t = 0) = \sin(2\pi(x + y)) \tag{26}$$

and the coordinate transformation function:

$$\begin{bmatrix} x \\ y \end{bmatrix} = \begin{bmatrix} D_x \cdot \cos(\theta) & -D_y \cdot \sin(\theta) \\ D_x \cdot \sin(\theta) & D_y \cdot \cos(\theta) \end{bmatrix} \begin{bmatrix} \xi \\ \eta \end{bmatrix} \tag{27}$$

Note that D_x and D_y are properly selected to ensure the state value consistent with the periodic boundaries. Fig. 6 shows the problem's initial and end state in the physical domain.

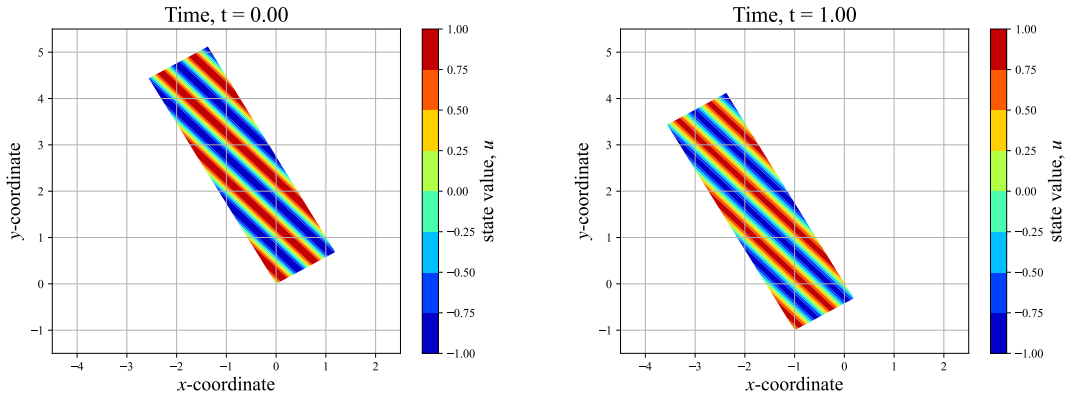

Fig. 6 Two-dimensional linear advection with a moving mesh: solution contours of the initial state (left) and the end state (right).

Fig. 7 shows the simulation results of the upwind finite difference method, MLC, and DMLC on the problem. In fifth-order methods, MLC and DMLC have very similar error distributions in the mesh number plot. Both of the MLC methods perform slightly better than the upwind finite difference method in terms of degrees of freedom and using less computing time to achieve the same order of accuracy. For seventh-order methods, all three methods have similar error distribution in terms of degrees of freedom with MLC deviating from the trending line for a few grid points. However, DMLC is still more efficient than the upwind finite difference. To obtain a result with L^1-norm error around 10^{-9}, the seventh-order DMLC took 54.7 seconds to complete and the seventh-order upwind finite difference method used 163.4 seconds which is 2.99 times speedup for DMLC.

D. Two-dimensional Supersonic Vorticity-Entropy Wave Interaction with a Shock Wave

This testing case aims to test the numerical accuracy of the MLC shock-fitting method proposed in section IV.C on the two-dimensional Euler equations. The problem is based on Mahesh's linear perturbation problem [18] which is a supersonic inviscid flow with a normal shock sitting in the middle of the computational domain ($x_G \approx 0$). Fig. 8 shows the initial density fluctuation distribution ($\rho^* = \rho'/A_e\overline{\rho}_1$) in the simulation domain. The left boundary is a supersonic inlet with a given Mach number M_∞ and the right boundary is a subsonic outlet. For the top and bottom boundaries, a periodic interface is applied to these boundaries to connect the simulation solutions on the horizontal borders virtually. The initial fluctuation terms for the upstream zone are applied as follows:

$$\begin{aligned} \frac{p_1'}{\overline{p}_1} &= 0 \\ \frac{u_1'}{\overline{u}_1} &= lA_v \cos(mx + ly - \overline{u}_1 mt) \\ \frac{v_1'}{\overline{u}_1} &= -mA_v \cos(mx + ly - \overline{u}_1 mt) \\ \frac{\rho_1'}{\overline{\rho}_1} &= A_e \cos(mx + ly - \overline{u}_1 mt) \end{aligned} \tag{28}$$

where $l = \sin(\psi_1)$ and $m = \cos(\psi_1)$. In this testing problem, the given freestream and fluctuation parameters are $M_\infty = 1.5$, $A_v = A_e = 10^{-4}$, and $\psi_1 = 15°$. For the initial solutions behind the shock wave, the downstream fluctuations

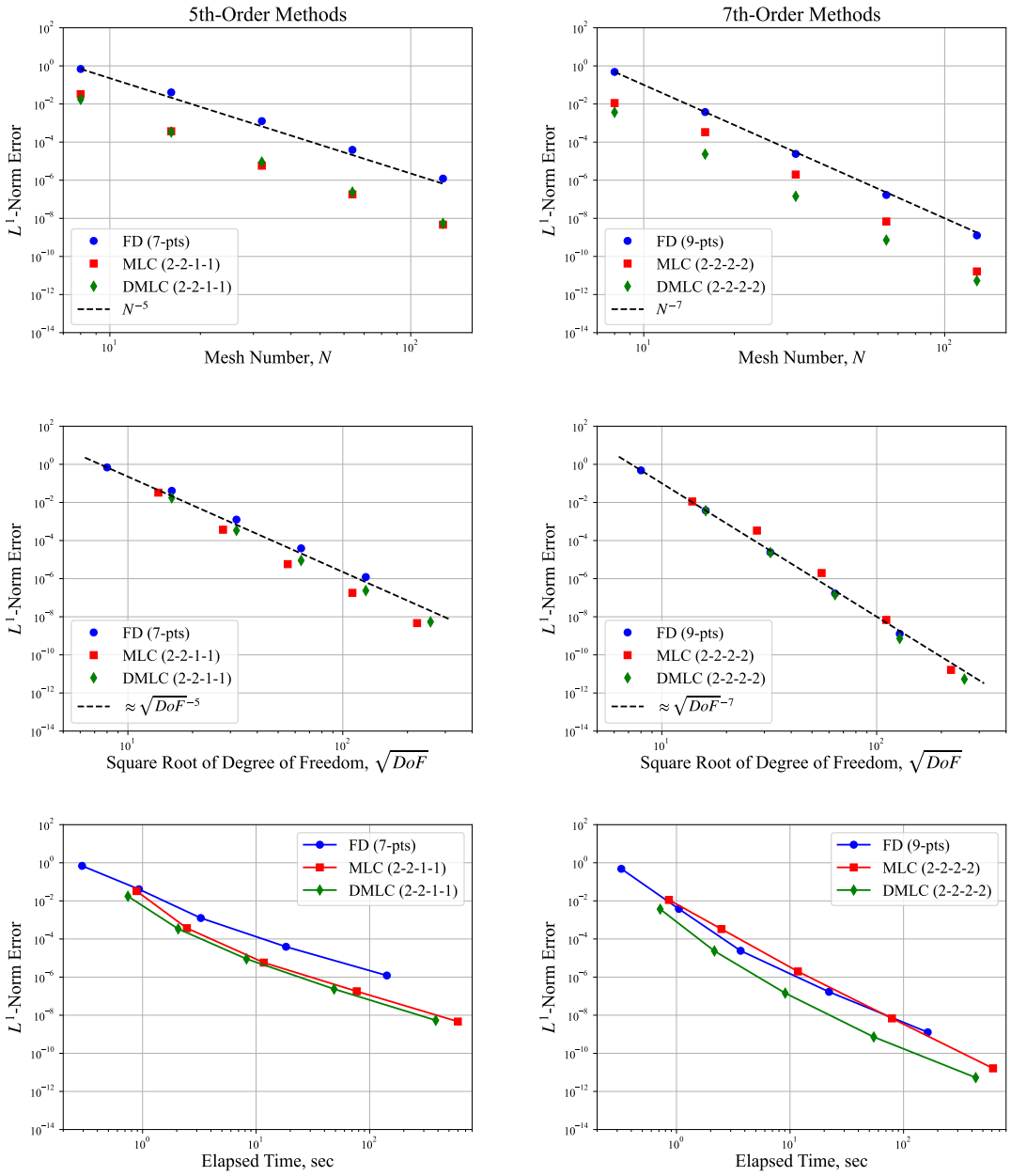

Fig. 7 Two-dimensional linear advection with a moving mesh: L^1-norm error versus mesh number N (top), degrees of freedom (middle), and computing elapsed time (bottom) for fifth (left) and seventh-order (right) methods.

and the shape of the shock wave are derived based on the linear perturbation theory. The linearized solution can be found in Mahesh's work [18]. For the numerical simulation setting, the subsonic outlet boundary condition is implemented by the non-reflecting characteristic boundary from Poinsot and Lele [19]. The entire computational domain is $\Omega = [-1.5\pi, 2\pi] \times [0, 2\pi)$ and is split into two zones: upstream and downstream. The number of grid points for each zone is $(N+1) \times N$. The third-order strong stability preserving Runge-Kutta method [20] is used for the time integration and the CFL number ranges from 0.05 to 0.3 for different grid sizes. The total simulation time is $T^* = T/T_{ref} \approx 6.95$ where the reference time is the perturbation traveling time in the spanwise direction, $T_{ref} = 2\pi l/\overline{u}_1 m$. The simulation time is set to prevent the outlet numerical error, a C^- acoustic wave, from reaching the solutions behind the shock wave.

Fig. 9 shows the L^1-norm error with different mesh sizes and orders of the method used. The error is computed

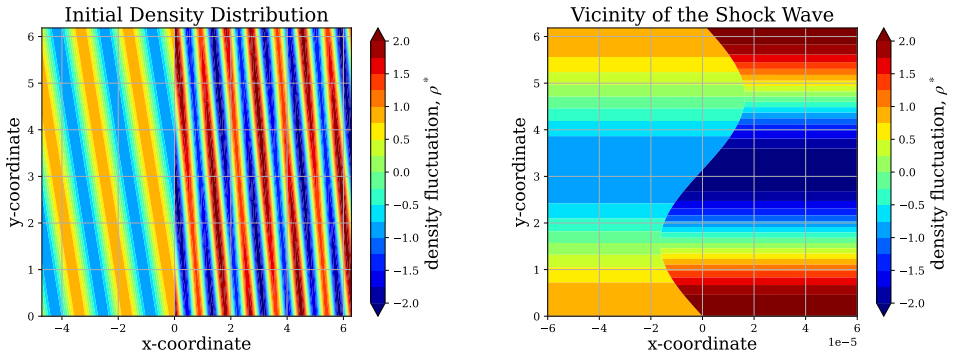

Fig. 8 Two-dimensional shock interaction: the initial density fluctuation distribution ($\rho^* = \rho'/A_e\rho_1$) in the entire computational domain (left) and in the vicinity of the shock wave (right).

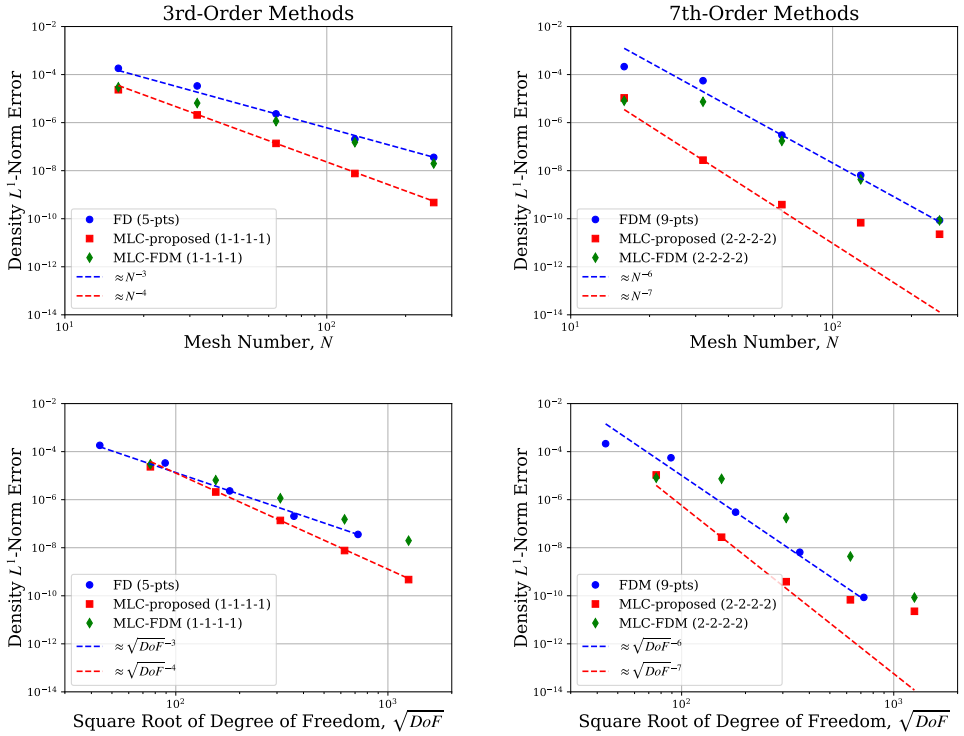

Fig. 9 Two-dimensional shock interaction: L^1-norm error versus mesh number N (top) and degree of freedom (bottom) for third (left) and seventh-order (right) methods.

based on the density error right behind the shock wave and the reference solution is the finest grid point solution ($N = 512$) from the seventh-order MLC. In addition to comparing the results between FD and MLC, this testing case also compares different boundary condition implementations for MLC for the stream-wise state derivative behind the shock wave $U_{s,\eta}$. The two boundary condition implementations are the method mentioned in section IV.C (MLC-proposed) and the finite difference method (MLC-FDM). The finite difference method uses $(r-1)$th-order one-sided difference scheme to estimate the derivative behind the shock from the downstream state values U. For seventh-order MLC, the finite difference approach uses $(r-2)$th-order (fifth-order) one-sided difference due to the numerical stability issue when sixth-order is used. Consequently, the L^1-norm error of the MLC-FDM is about the same as the FD for the same mesh number. On the other hand, the MLC-proposed approach can estimate the U_η derivative without using one-sided difference. This makes the method outperform the other two methods and achieve a seventh-order global

convergence rate for coarser grid points. The testing case shows the importance of the boundary condition used for the MLC to achieve the desired global convergence rate for simulation. The key to constructing an accurate MLC boundary condition is to ensure the condition's physical meaning between the value and derivative layers is consistent.

E. Two-dimensional Supersonic Flow over a Parabolic Cylinder

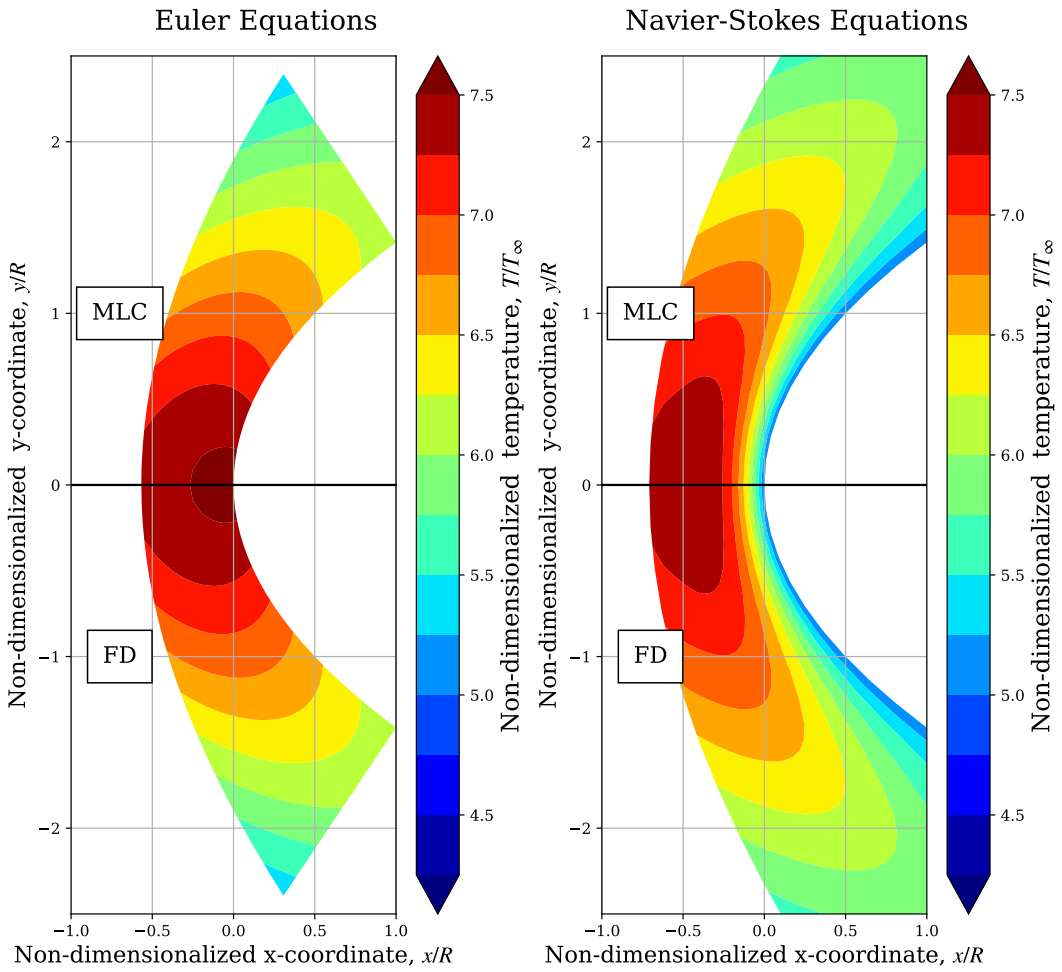

Fig. 10 Two-dimensional supersonic flow over parabolic cylinder: temperature contour for the Euler equations (left) and the Navier-Stokes equation (right) with third-order upwind finite difference method, FD, (lower section) and multi-layer compact scheme, MLC, (upper section).

The last simulation case is the two-dimensional supersonic flow over a parabolic cylinder. In this problem, both the Euler and Naver-Stokes equations are considered. For the geometry of the cylinder, the parabola is defined based on the radius of curvature at the parabola center R. The explicit wall's coordinate function is:

$$x_w = \frac{1}{2R} {y_w}^2 \tag{29}$$

The freestream flow conditions are $M_\infty = 5.73$, $Re_R = 100$, and $T_\infty = 250$. For simplicity, this problem only considers the ideal gas model with $\gamma = 1.4$ and $Pr = 0.77$. The rest of the flow conditions can be found in Zhong's supersonic over a cylinder study [2].

The tested schemes are the third-order FD (five-point stencil) and MLC (1-1-1-1) for this problem set. In the computational domain, ξ is defined as the clockwise azimuthal direction to the parabola, and η is defined as the wall-normal direction toward the shockfront. The parabola endpoints for the Euler equation are located at $x_{end} = R$ and

for the Navier-Stokes equations are $x_{end} = 4R$. The discrepancy in the domain size used for the two equations is due to the Navier-Stokes equations having convergence issues at the outlet for shorter computational domains. For boundary condition implementations, a mirror condition is used at the centerline to reduce the computational cost. The outlet boundary states in the Navier-Stokes simulations are computed through rth-order polynomial extrapolation for both value and derivative layers from the interior points. The inlet states are obtained from the shock-fitting method described in section IV. For the Euler wall boundary, the inviscid non-penetrable wall is applied. The pressure term is computed from the pressure gradient based on the momentum equation in the wall-normal direction. For the Navier-Stokes wall boundary, non-slip and isothermal conditions are applied. The wall temperature $T_w = 1250$ and the pressure term is extrapolated from the interior points. In addition, MLC uses polynomial extrapolation to obtain velocity derivatives on the wall. All of the simulations use third-order strong stability preserving Runge-Kutta method [20] for time integration with CFL number ranges from 0.05 to 0.6 for different mesh numbers. Simulations are considered converged when the non-dimensional velocity change over steps is less than 10^{-4}.

Fig. 10 shows the side-by-side comparison of the third-order FD and MLC in a non-dimensional temperature contour for the two equations with mesh number $(N_\xi, N_\eta) = (21, 21)$. The FD method is based on Zhong's work [2] which has been applied to various studies [21–23] and can be treated as the reference method to the problem. For the current implementation, the MLC has similar results as the FD which shows the solution consistency between the two methods. However, in Fig. 11, the L^1-norm error of the pressure for the MLC is less accurate than the FD for the same mesh number. This is due to the current MLC wall boundaries and subsonic outlet implementations are not physically consistent for both value and derivative layers. Most of the implementations rely on extrapolation or one-sided finite difference which introduces numerical instability or uncertainty to the MLC simulations. Also, as shown in the two-dimensional shock interaction case, a non-physically consistent boundary (MLC-FDM) will deteriorate MLC error convergence. As a result, deriving physically consistent boundary conditions for both wall boundary and subsonic outlet, such as MLC-proposed in the previous case, is necessary for MLC to achieve the desired order of accuracy globally.

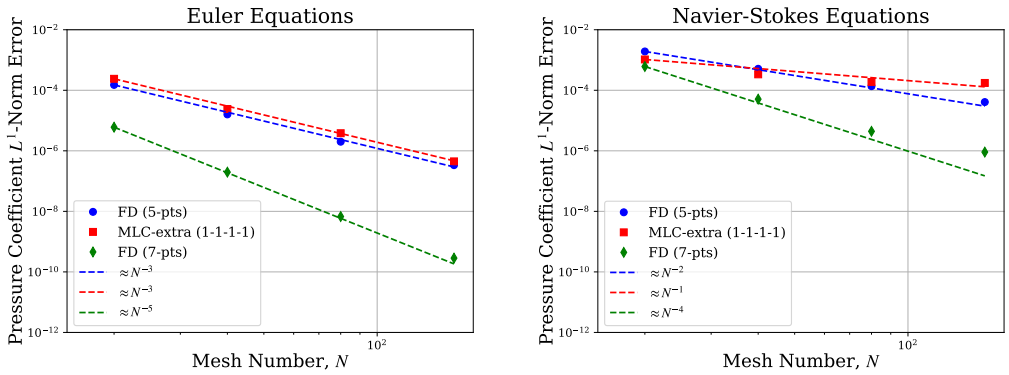

Fig. 11 Two-dimensional supersonic flow over parabolic cylinder: L^1-norm error for the pressure coefficient on the wall versus mesh number N for the Euler equations (left) and the Navier-Stokes equations (right).

VI. Conclusions and Future Work

This study implements the multi-layer compact scheme (MLC) on two-dimensional supersonic flow with non-Cartesian grids and uses the derivatives based on the computational domain U_ξ and U_η as the newly introduced degrees of freedom. In addition, a physically consistent boundary condition is proposed for the shock-fitting method. The numerical accuracy of combining MLC and the proposed boundary condition was investigated and compared with other high-order methods in both one-dimensional and two-dimensional problems. In the one-dimensional shock-density wave interaction problem, the approaches with the shock-fitting method have better spatial convergence rates than the shock-capturing methods. Shock-capturing methods only have around a first-order convergence rate for this problem. In contrast, the shock-fitting method can achieve sixth-order accuracy for the upwind finite difference method and eighth-order accuracy for MLC in the smooth region. This is due to the shock-fitting method only simulating the flow behind the shock wave which prevents the solution from smearing out and oscillating when across the discontinuous interface. Noting that, even though the shock-fitting method preserves high-order accuracy in this case, the method

requires a relatively simple shock structure to pre-define the shock location in the computational domain. For the fluid flow involved with complex and multiple shock interactions, shock-capturing methods are still the appropriate choice for these kinds of problems. Among the numerical schemes implemented with the shock-fitting method, MLC is more computationally efficient than the upwind finite difference for obtaining the same order of errors. The seventh-order MLC can have a 1.32 times speedup over the seventh-order upwind finite difference method for the same global L^1-norm error and 3.34 times speedup in the smooth region.

For the two-dimensional system, both MLC and DMLC were implemented on the linear advection with a moving mesh problem. The cross-derivative approximation in MLC makes the method less accurate in seventh-order form and potentially introduces numerical instability to the simulation. On the other hand, DMLC resolves the stability issue in approximating the cross-derivative term and has a more consistent and stable error convergence rate. The resulting speedup for DMLC over the finite difference method is 2.99. From the studied cases and compared methods, MLC is the suitable method for the one-dimensional problem and DMLC is the most efficient and stable method for the two-dimensional linear advection problem. In the two-dimensional shock interaction problem, the proposed MLC shock-fitting method is physically consistent between both value and derivative layers. This property stabilizes the MLC boundary scheme and makes the scheme achieve the desired order of accuracy globally. On the other hand, the current boundary condition implementations for the supersonic flow pass cylinder for both Euler and Navier-Stokes equations fail to achieve the desired order of accuracy. This is due to the wall boundary and subsonic outlet relying on polynomial extrapolation or one-sided difference which are not considered as physically consistent methods. These testing cases show the importance of consistency in MLC boundary conditions to fully utilize the method's potential.

The future work of this study is to derive the physically consistent wall boundaries and subsonic outlet for MLC. One of the approaches can be based on the high-order characteristic method from Poinsot and Lele [19]. The method provides a physically accurate description of the boundaries from the point of view of the method of characteristics. However, to apply the characteristic method to MLC on the parabolic cylinder, the non-Cartesian form of the method needs to be obtained. Also, the constraints for the MLC derivatives layer are required to be tested. If the physically consistent MLC boundary conditions are found for the supersonic flow pass cylinder problem, MLC potentially can achieve a global seventh-order convergence rate. With the correct boundary conditions, MLC will be able to significantly improve the simulation accuracy and computational efficiency of the supersonic boundary layer transition flow simulation which benefits the high-speed vehicle development in the aerospace research community.

Acknowledgments

Y.T. Lin thanks the Government Scholarship for Study Abroad (GSSA) from the Taiwan Ministry of Education for financially supporting the completion of this study.

References

[1] Wang, Z. J., Fidkowski, K., Abgrall, R., Bassi, F., Caraeni, D., Cary, A., Deconinck, H., Hartmann, R., Hillewaert, K., Huynh, H. T., et al., "High-order CFD methods: current status and perspective," *International Journal for Numerical Methods in Fluids*, Vol. 72, No. 8, 2013, pp. 811–845.

[2] Zhong, X., "High-order finite-difference schemes for numerical simulation of hypersonic boundary-layer transition," *Journal of Computational Physics*, Vol. 144, No. 2, 1998, pp. 662–709.

[3] Touber, E., and Sandham, N. D., "Large-eddy simulation of low-frequency unsteadiness in a turbulent shock-induced separation bubble," *Theoretical and Computational Fluid Dynamics*, Vol. 23, No. 2, 2009, pp. 79–107.

[4] Laible, A., and Fasel, H., "Numerical investigation of hypersonic transition for a flared and a straight cone at Mach 6," *41st AIAA Fluid Dynamics Conference and Exhibit*, 2011, p. 3565.

[5] Candler, G. V., Johnson, H. B., Nompelis, I., Gidzak, V. M., Subbareddy, P. K., and Barnhardt, M., "Development of the US3D code for advanced compressible and reacting flow simulations," *53rd AIAA Aerospace Sciences Meeting*, 2015, p. 1893.

[6] Li, X., Fu, D., and Ma, Y., "Direct numerical simulation of hypersonic boundary layer transition over a blunt cone," *AIAA journal*, Vol. 46, No. 11, 2008, pp. 2899–2913.

[7] Duan, L., Choudhari, M. M., and Wu, M., "Numerical study of acoustic radiation due to a supersonic turbulent boundary layer," *Journal of Fluid Mechanics*, Vol. 746, 2014, pp. 165–192.

[8] Bai, Z., and Zhong, X., "New very high-order upwind multi-layer compact (MLC) schemes with spectral-like resolution for flow simulations," *Journal of Computational Physics*, Vol. 378, 2019, pp. 63–109.

[9] Bai, Z., and Zhong, X., *New Very High-Order Upwind Multilayer Compact Schemes with Spectral-Like Resolution for Flow Simulations*, AIAA, 2017, Chaps. High-Order Methods I, pp. 1–42. https://doi.org/10.2514/6.2017-0518, URL https://arc.aiaa.org/doi/abs/10.2514/6.2017-0518.

[10] Bai, Z., and Zhong, X., "A new very high-order upwind directional multi-layer compact (DMLC) scheme for multi-dimensional flows," *Computers & Fluids*, Vol. 197, 2020, p. 104356.

[11] Persson, P.-O., Bonet, J., and Peraire, J., "Discontinuous Galerkin solution of the Navier–Stokes equations on deformable domains," *Computer Methods in Applied Mechanics and Engineering*, Vol. 198, No. 17-20, 2009, pp. 1585–1595.

[12] Rawat, P. S., and Zhong, X., "On high-order shock-fitting and front-tracking schemes for numerical simulation of shock–disturbance interactions," *Journal of Computational Physics*, Vol. 229, No. 19, 2010, pp. 6744–6780.

[13] Jiang, G.-S., and Shu, C.-W., "Efficient implementation of weighted ENO schemes," *Journal of computational physics*, Vol. 126, No. 1, 1996, pp. 202–228.

[14] Henrick, A. K., Aslam, T. D., and Powers, J. M., "Mapped weighted essentially non-oscillatory schemes: achieving optimal order near critical points," *Journal of Computational Physics*, Vol. 207, No. 2, 2005, pp. 542–567.

[15] Castro, M., Costa, B., and Don, W. S., "High order weighted essentially non-oscillatory WENO-Z schemes for hyperbolic conservation laws," *Journal of Computational Physics*, Vol. 230, No. 5, 2011, pp. 1766–1792.

[16] Shu, C.-W., and Osher, S., "Efficient implementation of essentially non-oscillatory shock-capturing schemes, II," *Upwind and High-Resolution Schemes*, Springer, 1989, pp. 328–374.

[17] Suresh, A., "Interaction of a shock with a density disturbance via shock fitting," *Journal of Computational Physics*, Vol. 206, No. 1, 2005, pp. 6–15.

[18] Mahesh, K., *The interaction of a shock wave with a turbulent shear flow*, Stanford University, 1996.

[19] Poinsot, T. J., and Lelef, S., "Boundary conditions for direct simulations of compressible viscous flows," *Journal of computational physics*, Vol. 101, No. 1, 1992, pp. 104–129.

[20] Gottlieb, S., and Shu, C.-W., "Total variation diminishing Runge-Kutta schemes," *Mathematics of computation*, Vol. 67, No. 221, 1998, pp. 73–85.

[21] Knisely, C. P., and Zhong, X., "Sound radiation by supersonic unstable modes in hypersonic blunt cone boundary layers. II. Direct numerical simulation," *Physics of Fluids*, Vol. 31, No. 2, 2019.

[22] Haley, C., and Zhong, X., "Supersonic mode in a low-enthalpy hypersonic flow over a cone and wave packet interference," *Physics of Fluids*, Vol. 33, No. 5, 2021.

[23] He, S., and Zhong, X., "The effects of nose bluntness on broadband disturbance receptivity in hypersonic flow," *Physics of Fluids*, Vol. 34, No. 5, 2022.